Article

Thermal- and Photoinduced Spin-State Switching in an Unprecedented Three-Dimensional Bimetallic Coordination Polymer

NIEL, Virginie, *et al*.

Abstract

The compound {Fe(pmd)[Ag(CN)2][Ag2(CN)3]} (pmd=pyrimidine) was synthesized and characterized. Magnetic, calorimetric and single crystal visible spectroscopic studies demonstrate the occurrence of a two-step high-spin (HS) low-spin (LS) transition. The critical temperatures are Tc1=185 and Tc2=148 K. Each step involves 50 % of the iron centers, with the low-temperature step showing a hysteresis of 2.5 K. The enthalpy and entropy variations associated with the two steps are H1=3.6±0.4 kJ mol-1 and S1=19.5±3 J K-1 mol-1; H2=4.8±0.4 kJ mol-1 and S2=33.5±3 J K-1 mol-1. Photomagnetic and visible spectroscopy experiments show that below 50 K, where the LS state is the thermodynamically stable state, the compound can be switched quantitatively to the HS state using green-red light (550-650 nm). HS-to-LS relaxation experiments in the dark at temperatures between 15 and 55 K show that the relaxation takes place via a two-step cooperative process, which was analyzed in the context of the mean field theory. The crystal structure has been studied at 290, 220, 170, 90 and 30 K together with 30 K after irradiation. The compound [...]

Reference

UNIVERSITÉ
DE GENÈVE

Thermal- and Photoinduced Spin-State Switching in an Unprecedented Three-Dimensional Bimetallic Coordination Polymer

Virginie Niel,[a] Amber L. Thompson,[b] Andrés E. Goeta,*[b] Cristian Enachescu,[c] Andreas Hauser,*[c] Ana Galet,[d] M. Carmen Muñoz,[d] and José A. Real*[a]

Dedicated to Professor Philipp Gütlich on the occasion of his 70th birthday

Abstract: The compound {Fe(pmd)[Ag(CN)$_2$][Ag$_2$(CN)$_3$]} (pmd = pyrimidine) was synthesized and characterized. Magnetic, calorimetric and single crystal visible spectroscopic studies demonstrate the occurrence of a two-step high-spin (HS) $\rightleftarrows$ low-spin (LS) transition. The critical temperatures are $T_{c1} = 185$ and $T_{c2} = 148$ K. Each step involves ~50% of the iron centers, with the low-temperature step showing a hysteresis of 2.5 K. The enthalpy and entropy variations associated with the two steps are $\Delta H_1 = 3.6 \pm 0.4$ kJ mol^{-1} and $\Delta S_1 = 19.5 \pm 3$ J K^{-1} mol^{-1}; $\Delta H_2 = 4.8 \pm 0.4$ kJ mol^{-1} and $\Delta S_2 = 33.5 \pm 3$ J K^{-1} mol^{-1}. Photomagnetic and visible spectroscopy experiments show that below 50 K, where the LS state is the thermodynamically stable state, the

compound can be switched quantitatively to the HS state using green-red light (550–650 nm). HS-to-LS relaxation experiments in the dark at temperatures between 15 and 55 K show that the relaxation takes place via a two-step cooperative process, which was analyzed in the context of the mean field theory. The crystal structure has been studied at 290, 220, 170, 90 and 30 K together with 30 K after irradiation. The compound adopts monoclinic symmetry ($P2_1/c$, $Z = 16$) at all temperatures. There are five [FeN$_6$] pseudo-octahedral sites linked by pmd,

[Ag(CN)$_2$]$^-$ and [Ag$_2$(CN)$_3$]$^-$ bridging ligands to form an unprecedented three-dimensional (6,6) topology. The structural analysis allows for an understanding of the microscopic mechanism of the two-step behavior of the thermally induced spin transition as well as the corresponding relaxation of the photoexcited compound based on the individual changes of the five sites. Synergy between metallophilic interactions and the spin transition is also shown by the variation of the Ag···Ag distances. Correlations between the variation of the unit-cell volume and the change of Ag···Ag interactions within each step with the asymmetric change of the anomalous heat capacity have also been inferred.

Keywords: argentophilic interactions · coordination modes · polymers · spin crossover

Introduction

Iron(II) spin crossover (SCO) solids are molecule based compounds, commutable between two states in thermodynamic competition: the paramagnetic high-spin state (HS) is

stable at high temperatures and the diamagnetic low-spin state (LS) is stable at low temperatures. The two states not only have different magnetic properties, but also different structural and optical properties. Structurally, these two states are characterized by Fe–N bond lengths of around 2.2

[a] Dr. V. Niel, Prof. Dr. J. A. Real
Institut de Ciencia Molecular/Departament de Química Inorgánica
Universitat de València, Doctor Moliner 50
46100 Burjassot (Spain)
Fax: (+34) 963-544-856
E-mail: jose.a.real@uv.es

[b] Dr. A. L. Thompson, Dr. A. E. Goeta
Department of Chemistry, University of Durham
South Road, Durham DH1 3LE (UK)
E-mail: a.e.goeta@durham.ac.uk

[c] Dr. C. Enachescu, Prof. Dr. A. Hauser
Département de chimie physique
Université de Genève, 30 quai Ernest-Ansermet
1211 Genève (Switzerland)
E-mail: andreas.hauser@chiphy.unige.ch

[d] A. Galet, Prof. Dr. M. C. Muñoz
Departament de Física Aplicada
Universitat Politècnica de València
Camino de Vera s/n, 46071, Valencia (Spain)

Supporting information for this article is available on the WWW under http://www.chemeurj.org/ or from the author and includes additional structural data, relaxation curves obtained from magnetic susceptibility data after LIESST effect at 40, 44, 50 and 52 K, and variable temperature powder diffraction data.

and 2.0 Å for the HS and LS states, respectively. However, it is also common to refer to the octahedral volume around the iron centers (~13 Å^3 for HS and ~10 Å^3 for LS), as this also takes into account differences in geometry. Switching between the two states may be stimulated by a change of temperature, pressure or by illumination with light. Often, cooperative interactions of elastic origin result in abrupt thermal spin transitions and the presence of hysteresis, which confer to these materials a memory effect.[1] All these features make iron(II) SCO building blocks particularly suitable for the construction of multi-property materials in which SCO may be combined with other interesting properties, for instance, inclusion phenomena, magnetic exchange or allosterism.

Cyanide-bridged homo- and heterometallic polymers have been shown to exhibit a remarkable diversity of structural types with interesting magnetic, electrochemical, magneto-optical and zeolitic properties.[2] In particular, Hofmann-like clathrate compounds[3] containing iron(II) ions have led to the development of a number of two- and three-dimensional polymeric SCO networks such as {Fe(L)$_x$[M^{II}(CN)$_4$]}·n H$_2$O [L=pyridine, x=2, n=0;[4] L=pyrazine, x=1, n=2 (n=2.5 for Pd),[5] M^{II}=Ni, Pd, Pt], which display abrupt thermal and pressure induced transitions and hysteresis at temperatures close to room temperature.[6] The formal replacement of the [M^{II}(CN)$_4$]$^{2-}$ anions by [M^{I}(CN)$_2$]$^-$ groups (M^{I}=Cu, Ag, Au), with *trans*-bispyridylethylene, 4,4′-bipyridine, 3CN-pyridine or pyrimidine (pmd) as ligands, has resulted in new 2D and double or triple interpenetrated 3D SCO polymers.[7] Such compounds combine cooperative SCO properties (magnetic, chromatic and structural) with different chemical properties such as specific host–guest interactions as in {Fe(pyrazine)[M^{II}(CN)$_4$]}·solvent,[8] crystalline-state reactions with allosteric effects as in {Fe(pmd)(H$_2$O)-[M^{I}(CN)$_2$]$_2$}·H$_2$O,[7c] or SCO tuned metallophilicity as in {Fe(3-CNpyridine)[Ag(CN)$_2$]$_2$}·$\frac{1}{3}$H$_2$O.[7d] In summary, these materials offer the opportunity to investigate the interplay between different molecular and/or supramolecular components and the collective properties that may arise from the synergy between the individual component properties.

As a new step in this research, we present herein the synthesis and crystal structures (recorded at 290, 220, 170, 90 and 30 K) as well as the magnetic, calorimetric, and optical properties of a novel thermally and optically switchable SCO coordination polymer {Fe(pmd)[Ag(CN)$_2$][Ag$_2$(CN)$_3$]}. In addition to the remarkable physical properties, {Fe(pmd)-[Ag(CN)$_2$][Ag$_2$(CN)$_3$]} also exhibits an unprecedented 3D topology and strong argentophilic interactions which are intrinsically linked to the SCO. The crystal structure of the photoinduced metastable HS spin state (of which just a handful of only mononuclear compounds have been reported to date),[9] is also reported together with the corresponding HS-to-LS relaxation kinetics monitored using magnetic and visible spectroscopy measurements. The two-step character of the thermal-induced SCO and relaxation process is analyzed phenomenologically by using appropriate models according to the microscopic mechanism deduced from the thorough structural analysis of this singular polymer.

Results and Discussion

Synthesis: As described in the Experimental Section, the synthesis of the title compound results in a mixture of two very different crystalline phases. These phases have very different structural and physical properties, and those for {Fe(pmd)(H$_2$O)[Ag(CN)$_2$]$_2$}·H$_2$O will not be discussed here in detail since they have been published previously elsewhere.[7c] However, it is worth mentioning that one of the key characteristics of this compound is its ability to undergo a controlled and fully reversible crystalline-state ligand substitution, involving reversible coordination/uncoordination of gaseous water and pmd.

In spite of the low yield of the title compound {Fe(pmd)-[Ag(CN)$_2$][Ag$_2$(CN)$_3$]}, its synthesis is perfectly reproducible and relatively large amounts may be obtained. The very different texture and size make it easy to separate the crystals of the title compound from those of the other compound, especially as they grow in quite different parts of the H-shaped diffusion vessel.

In addition to elemental analysis, the purity of the samples can be independently checked from the temperature dependence of the magnetic susceptibility, anomalous heat capacity and electronic spectroscopy (visible spectroscopy). Given that {Fe(pmd)(H$_2$O)[Ag(CN)$_2$]$_2$}·H$_2$O undergoes a very sharp SCO transition at a well defined temperature (centered at 219 K with a 8 K hysteresis), even very small amounts of this compound (1–2%) would be detected in the massive samples used for magnetic, photomagnetic and calorimetric measurements of the title compound. Such signals have not been observed.

Besides its singular magnetic and structural properties, the main difference between the title compound and {Fe(pmd)(H$_2$O)[Ag(CN)$_2$]$_2$}·H$_2$O is the occurrence of the relatively rare [Ag$_2$(CN)$_3$]$^-$ anion. This species has been previously identified by Brunner,[10] Iwamoto[11] and Leznoff[12] and co-workers in crystals of coordination polymers. However, the species [Ag$_2$(CN)$_3$]$^-$ has never been observed in solution or isolated in crystals of single salts. The formation of this species requires some degree of lability in the thermodynamically stable precursor [Ag(CN)$_2$]$^-$; its overall formation constant is $\beta_2 = 10^{20.44}$.[13] According to Leznoff and co-workers the incorporation of [Ag(CN)$_2$]$^-$ and [Ag$_2$(CN)$_3$]$^-$ into the final polymer is the result of competition between the two moieties and their associated equilibria. This competition is influenced by the solvent medium, reagent concentrations and overall stability and solubility of the final product. In the present case, the diffusion method creates appropriate conditions, that is, low concentration of [Ag(CN)$_2$]$^-$ and extended reaction time, which favors the dissociation of [Ag(CN)$_2$]$^-$ to give [Ag$_2$(CN)$_3$]$^-$. In this respect, it is worth noting that while the isostructural gold analogue of {Fe(pmd)(H$_2$O)[Ag(CN)$_2$]$_2$}·H$_2$O can easily be iso-

lated, the compound {Fe(pmd)[Au(CN)$_2$][Au$_2$(CN)$_3$]} has not yet been isolated. This fact is in agreement with the comparative studies dealing with the lability of aqueous Au^I and Au^I cyanide complexes.[14]

Magnetic and photomagnetic measurements: Figure 1 shows the thermal dependence of the $\chi_M T$ product (black diamonds) of the title compound as a function of temperature, where χ_M is the molar magnetic susceptibility and T is the temperature. At 300 K, $\chi_M T$ is equal to 3.54 cm^{3}K mol^{-1}, which is within the range of values expected for iron(II) ions in the HS state. As the temperature is lowered, $\chi_M T$ initially remains almost constant and then starts to decrease quite steeply below 225 K to a value of 1.85 cm^{3}K mol^{-1} at 175 K. The critical temperature for this step is $T_{c1}=185$ K. In the temperature range 177–155 K, $\chi_M T$ varies very smoothly around the value of 1.80 cm^{3}K mol^{-1} and defines a plateau involving about 50 % of iron(II) atoms (HS molar fraction $\gamma_{HS} \approx 0.5$). For temperatures below 155 K, $\chi_M T$ experiences a new sharp drop and reaches a value of 0.15 cm^{3}K mol^{-1} at 130 K, which indicates that the SCO is virtually complete. The magnetic behavior in the warming and cooling modes indicates the occurrence of a narrow hysteresis loop about 1.5 K wide for the low-temperature step, with critical temperatures $T_{c2}\downarrow=146$ K and $T_{c2}\uparrow=147.5$ K, and no appreciable thermal hysteresis for the high-temperature step.
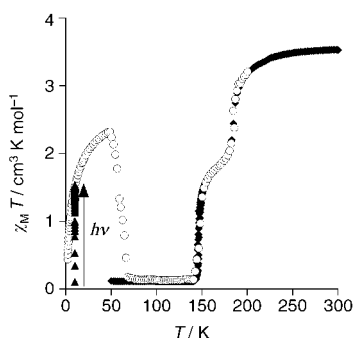

Figure 1. $\chi_M T$ versus T plots for the title compound: cooling and warming modes (♦), following irradiation (LIESST effect) at 10 K (▲) and warming of the photoexcited sample from 2 K up to 200 K (○).

Photogeneration of the metastable HS state at low temperatures, the so-called Light-Induced Excited Spin-State Trapping (LIESST) experiment,[15] was carried out on a microcrystalline sample (0.46 mg). The results are displayed in Figure 1. As before, the magnetic response was measured in the cooling mode (cooling rate 2 K min^{-1}) from 300 K down to 10 K with an applied magnetic field of 1.5 T (black diamonds). At 10 K, the sample was irradiated with green light (550 nm) for 150 min, the time required to reach a saturation value of $\chi_M T \approx 1.63$ cm^{3}K mol^{-1} (triangles), which apparently represents about 46 % of LS→HS conversion, from comparison with the room temperature value of $\chi_M T$. The light irradiation was then switched off, and the temperature was first decreased to 2 K and then increased to 200 K at

0.5 K min^{-1}. In the temperature region 2–48 K, $\chi_M T$ increases up to a value of 2.35 cm^{3}K mol^{-1} (open circles). This increase of $\chi_M T$ indicates a thermal population of the different microstates arising from zero-field splitting of the $S=2$ excited state and/or weak iron(II)–iron(II) antiferromagnetic interactions, which is expected to occur in the one-dimensional single-bridged [Fe(pmd)]$_\infty$ chains (see below).[16] This fact suggests that the light-induced population of the HS state is virtually complete at 10 K. At temperatures greater than 40 K, $\chi_M T$ drops rapidly in two steps to reach a value close to 0.25 cm^{3}K mol^{-1} at 60 K, indicating the occurrence of a complete HS→LS relaxation. This relaxation process, studied at different temperatures in the SQUID magnetometer (see Supporting Information) agrees quite well with that monitored by means of visible spectroscopy and that performed on a small single crystal (see below).

Crystallography: The crystal structure of the title compound was studied at 290, 220, 170, 90, 30 and at 30 K after irradiation with red light ($\lambda=633$ nm). The compound crystallizes in the monoclinic system ($P2_1/c$, $Z=16$) and does not change symmetry irrespective of temperature and light irradiation. Crystal and refinement data can be found in Table 1. The structural motifs in this material are essentially the same at all temperatures, with changes in bond lengths and angles in keeping with the characteristic structural changes of the spin transition. Consequently, during the description of the structural features at temperatures other than 290 K, the emphasis is put on these changes.

Crystal structure at 290 K: The crystal structure consists of an intricate 3D net, whose knots are defined by five crystallographically inequivalent iron atoms. With $Z=16$, there are five crystallographically independent iron atoms in the asymmetric unit of which two [Fe(4) and Fe(5)] are located on inversion centers. Thus, in the asymmetric unit there is a total of four iron atoms: three full iron atoms [Fe(1), Fe(2) and Fe(3)] and half of Fe(4) and Fe(5). All five iron atoms lie at the center of strongly distorted [FeN$_6$] coordination units. The equatorial bond lengths (Fe–N$_{eq}$) are defined by the nitrogen atoms of the [Ag(CN)$_2$]$^-$ and [Ag$_2$(CN)$_3$]$^-$ groups and are shorter than those of the axial bond lengths (Fe–N$_{ax}$, see Supporting Information and Table 2). The axial positions are occupied by the nitrogen atoms of the pmd groups, which act as bridging ligands between iron centers, forming chains (see Figures 2 and 3). The average Fe–N distances of 2.13–2.18 Å are consistent with the HS state as observed from the magnetic data at 290 K. Consequently, all five non-equivalent iron atoms have very similar octahedral volumes (see Table 3),[17] which are within the expected range found for other high spin FeN$_6$ octahedrons.[9a,c]

The five different iron atoms in the asymmetric unit present different coordination "motifs". Each iron atom has a different number and arrangement of the [Ag(CN)$_2$]$^-$ and [Ag$_2$(CN)$_3$]$^-$ anions around it, which connect the iron atoms together in a complex way (see Figure 2). One of the most important points regarding this connectivity is that Fe(5) is

Table 1. Crystallographic data. The values for 30i and all other tables refer to data collected at 30 K after irradiation, see text for further information.

T [K]	290	220	170	90	30	30i
empirical formula			$C_9H_4N_7Ag_3Fe$			
formula weight			589.65			
λ [Å]			0.71073			
space group			$P2(1)/c$			
a [Å]	17.5612(6)	17.5674(4)	17.2546(5)	17.1811(6)	17.176(6)	17.584(3)
b [Å]	29.2365(10)	29.2216(7)	29.5187(10)	29.2656(11)	29.235(10)	29.254(5)
c [Å]	12.2971(5)	12.2541(3)	11.9267(5)	11.5837(5)	11.553(4)	12.182(2)
β [°]	97.399(2)	97.3020(10)	96.909(2)	97.080(2)	96.952(10)	97.042(4)
V [Å³]	6261.1(4)	6239.6(3)	6030.6(4)	5780.0(4)	5759(3)	6219.1(19)
Z			16			
μ [mm⁻¹]	4.603	4.619	4.779	4.986	5.005	4.634
ρ_{calcd} [g cm⁻³]	2.502	2.511	2.598	2.710	2.720	2.519
R_{int}	0.0539	0.0488	0.0636	0.0614	0.0568	0.0675
total no. reflns	20590	20448	20152	19203	8279	12844
final R indices [$I > 2\sigma(I)$]						
R_1	0.0476	0.0439	0.0587	0.0537	0.0950	0.1025
wR_2	0.0814	0.0770	0.1212	0.1276	0.1579	0.1749
final R indices [all data]						
R_1	0.1562	0.1227	0.1376	0.0963	0.1390	0.1499
wR_2	0.1005	0.0911	0.1411	0.1398	0.1791	0.1969

Table 2. Average Fe–N distances at the different temperatures [Å].

T [K]	290	220	170	90	30	30i
Fe(1)−N$_{eq}$	2.15(1)	2.14(1)	2.02(1)	1.94(1)	1.96(1)	2.14(1)
Fe(1)−N$_{ax}$	2.23(1)	2.22(1)	2.08(1)	1.99(1)	2.01(1)	2.19(2)
Fe(2)−N$_{eq}$	2.14(1)	2.14(1)	2.13(1)	1.94(1)	1.94(1)	2.14(1)
Fe(2)−N$_{ax}$	2.24(1)	2.23(1)	2.23(1)	2.02(1)	1.99(1)	2.23(1)
Fe(3)−N$_{eq}$	2.13(1)	2.13(1)	1.95(1)	1.94(1)	1.93(1)	2.13(1)
Fe(3)−N$_{ax}$	2.22(1)	2.20(1)	1.99(1)	1.99(1)	2.00(1)	2.20(1)
Fe(4)−N$_{eq}$	2.13(1)	2.13(1)	2.13(1)	1.94(1)	1.97(1)	2.12(1)
Fe(4)−N$_{ax}$	2.21(1)	2.23(1)	2.20(1)	1.99(1)	2.00(1)	2.27(1)
Fe(5)−N$_{eq}$	2.11(1)	2.05(1)	1.92(1)	1.92(1)	1.93(1)	1.93(1)
Fe(5)−N$_{ax}$	2.19(1)	2.14(1)	1.98(1)	2.00(1)	1.97(1)	2.00(1)

Table 3. Volumes of the FeN$_6$ octahedrons around each crystallographically inequivalent Fe atom and at each measured temperature [Å³].

T [K]	290	220	170	90	30	30i
Fe(1)	13.69	13.58	11.33	9.95	10.19	13.23
Fe(2)	13.62	13.54	13.40	10.07	10.00	13.55
Fe(3)	13.38	13.27	10.01	9.95	9.85	13.30
Fe(4)	13.43	13.49	13.26	9.93	10.26	13.61
Fe(5)	12.94	12.00	9.72	9.80	9.76	9.98

connected solely to Fe(3) through all four of its silver cyanide ligands. The anionic groups $[Ag(CN)_2]^-$ and $[Ag_2(CN)_3]^-$, defined by the twelve crystallographically different silver atoms, display geometries close to linear. The average Fe⋯Fe distance through $[Ag(CN)_2]^-$ and $[Ag_2(CN)_3]^-$ is 10.16(15) and 15.62(9) Å, respectively.

The pmd bridges and the iron atoms form -[Fe-pmd-Fe]$_∞$- chains running along the c axis (Figure 3a). There are three different kinds of -[Fe-pmd-Fe]$_∞$- chains in the structure: -[Fe(1)-pmd-Fe(1)]$_∞$-, -[Fe(2)-pmd-Fe(3)]$_∞$- and -[Fe(4)-pmd-

Fe(5)]$_∞$-. The chain formed by only equivalent Fe(1) iron atoms (-[Fe(1)-pmd-Fe(1)]$_∞$-) has an Fe(1)⋯Fe(1) distance of 6.1489(3) Å. The other two -[Fe-pmd-Fe]$_∞$- chains are formed by two inequivalent alternating iron atoms: -[Fe(2)-pmd-Fe(3)]$_∞$- with Fe(2)⋯Fe(3) 6.174(2) Å and Fe(3)⋯Fe(2) 6.155(2) Å in one case, and -[Fe(4)-pmd-Fe(5)]$_∞$- with Fe(4)⋯Fe(5) = Fe(5)⋯Fe(4) 6.1485(3) Å in the other. In addition, Fe(1)–Fe(1) and Fe(4)–Fe(5) chains alternate along the direction of the b axis, defining 2D sheets of iron atoms lying in the bc plane. These layers alternate along the a axis with similar 2D sheets formed only of Fe(2)–Fe(3) chains, (Figure 3a). The layers formed by the different -[Fe-pmd-Fe]$_∞$- chains are organized such that chains in consecutive layers are shifted along the b axis by approximately half the interchain separation (around 3.55 Å for all temperatures).

The adjacent iron layers are connected through $[Ag(CN)_2]^-$ and $[Ag_2(CN)_3]^-$ bridges. They can also be seen as separated by dense layers of Ag atoms (Figure 3b), where strong argentophilic interactions are observed. These ligand unsupported Ag⋯Ag interactions define linear trinuclear, angular trinuclear and hexanuclear moieties (see Figure 4). The shortest Ag⋯Ag distances between $[Ag(CN)_2]^-$ and $[Ag_2(CN)_3]^-$ are in the range 2.98–3.02 Å (see Table 4), only slightly longer than that in Ag metal (2.89 Å).[18]

The title compound formally has a close relationship with $\{Cd(pz)[Ag(CN)_2][Ag_2(CN)_3]\}$ (pz=pyrazine), which was reported by Iwamoto and co-workers.[11] This compound is made up of an infinite stack of parallel $\{Cd[Ag(CN)_2][Ag_2(CN)_3]\}_∞$ layers in which the rectangular motifs $\{Cd[Ag(CN)_2][Ag_2(CN)_3]\}_4$ define the grids of the frame. The layers are stacked one on top of each other and connected by the pz bridges through axial coordination of the Cd^{II} ions, defining a porous 3D network. The empty space
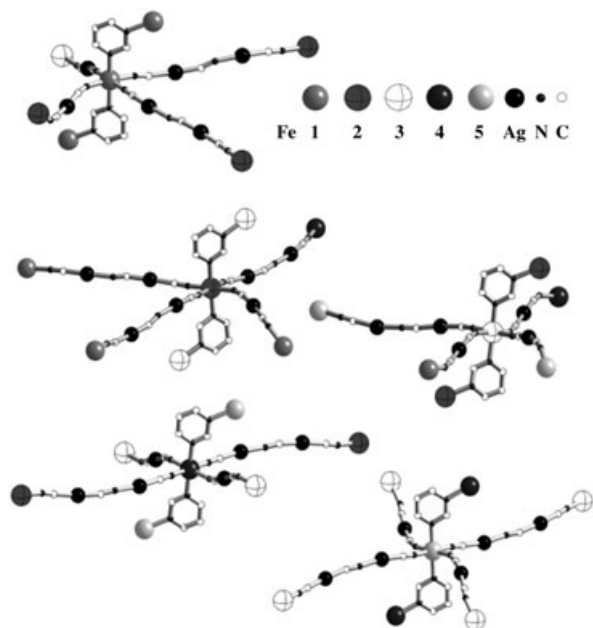
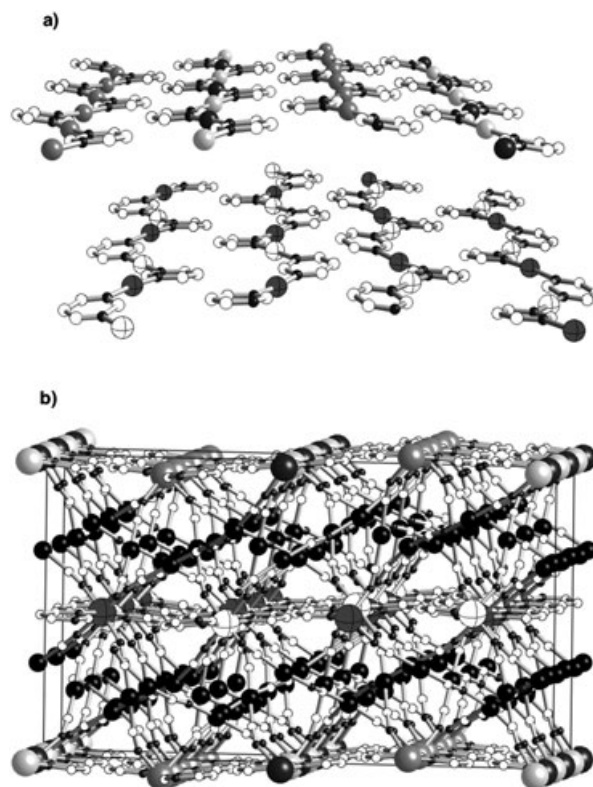Figure 2. Coordination environments of the five crystallographically inequivalent Fe atoms.

Figure 3. a) View of the -[Fe-pmd-Fe]$_\infty$- chains running along the c axis. b) View of the packing down the c axis. Hydrogen atoms have been omitted for clarity.

allows the triple interpenetration of three additional identical networks (Figure 5a). In contrast, the title compound {Fe(pmd)[Ag(CN)$_2$][Ag$_2$(CN)$_3$]}$_\infty$ defines a 3D network with a very complex topology, where the pmd group plays the role of an auxiliary bridging ligand. However, the pmd ligands play an essential role in the conformation of the framework, as the *meta* (or 1,3) disposition of their donor nitrogen atoms imposes a particular orientation on the basal coordination planes [Fe-(NCAg-)$_4$]. Thus, the dihedral angle between two consecutive [Fe-(NCAg-)$_4$] planes is about 62° instead of 0° as seen in the pz derivative (see Figure 5b). This arrangement of the [Ag(CN)$_2$]$^-$ and [Ag$_2$(CN)$_3$]$^-$ ligands in the equatorial coordination plane, together with the five different Fe centers, generates an intricate network, which can be considered as self-interpenetrated. The connectivity of a particular chain, for example, -[Fe(2)-pmd-Fe(3)]$_\infty$-, to four other chains (-[Fe(1)-pmd-Fe(1)]$_\infty$- and -[Fe(4)-pmd-Fe(5)]$_\infty$-), shows the (6,6) topology of the network (Figure 6a).[19] Each approximately rectangular circuit {(Fe(2)-pmd-Fe(3)-pmd-Fe(2))$_2$-L$_2$} and {(Fe(3)-pmd-Fe(2)-pmd-Fe(3))$_2$-L$_2$} (where L=[Ag(CN)$_2$]$^-$ or [Ag$_2$(CN)$_3$]$^-$), radiates in a different direction towards the surrounding chains. These circuits are interpenetrated by other circuits defined by adjacent -[Fe-pmd-Fe]$_\infty$- chains and [Ag(CN)$_2$]$^-$/ [Ag$_2$(CN)$_3$]$^-$ groups (see Figure 6b). To the best of our knowledge, the structure of the
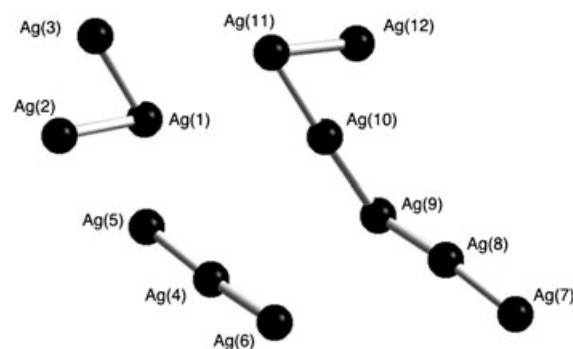

Figure 4. Ligand unsupported argentophilic interactions.

Table 4. Shortest Ag–Ag contacts at the different temperatures [Å].

| Species	Distances [Å]	T [K]					
		290	220	170	90	30	30i
trinuclear	Ag(1)···Ag(2)	3.242(2)	3.226(2)	3.184(3)	3.096(2)	3.087(3)	3.166(3)
angular	Ag(1)···Ag(3)	3.268(2)	3.260(2)	3.262(3)	3.257(2)	3.238(3)	3.214(3)
trinuclear	Ag(4)···Ag(5)	2.993(2)	2.991(2)	2.963(3)	2.942(2)	2.936(3)	3.003(3)
linear	Ag(4)···Ag(6)	2.997(2)	2.988(2)	2.975(3)	2.945(2)	2.946(3)	2.981(3)
	Ag(7)···Ag(8)	3.015(2)	3.017(2)	3.017(3)	2.942(2)	2.934(3)	3.025(3)
	Ag(8)···Ag(9)	2.984(2)	2.987(2)	2.983(3)	2.944(2)	2.940(3)	2.997(3)
hexanuclear	Ag(9)···Ag(10)	3.202(2)	3.187(2)	3.180(3)	3.153(2)	3.141(3)	3.150(3)
	Ag(10)···Ag(11)	3.286(2)	3.260(2)	3.196(3)	3.106(2)	3.097(3)	3.200(3)
	Ag(11)···Ag(12)	3.235(2)	3.217(2)	3.223(3)	3.159(2)	3.141(3)	3.164(3)
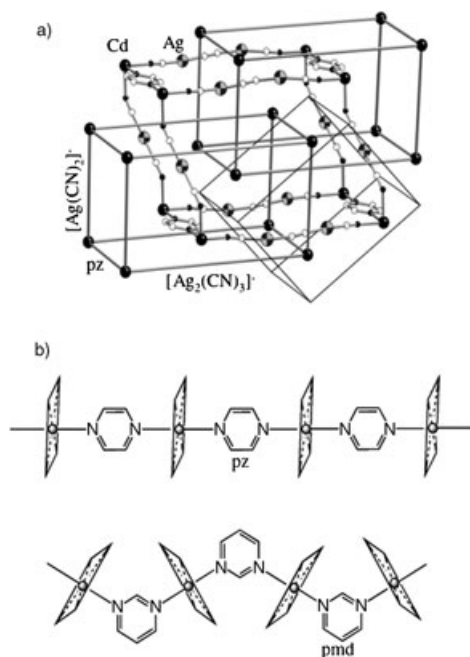
Figure 5. a) Triple interpenetrated networks in {Cd(pz)[Ag(CN)$_2$] [Ag$_2$(CN)$_3$]} (pz = pyrazine).[18] b) Different arrangement of the basal coordination planes [Fe-(NCAg-)$_4$] in {Cd(pz)[Ag(CN)$_2$][Ag$_2$(CN)$_3$]} and the title compound.

title compound provides the first example of a new type of 3D four-connected net, in which the zig-zag nature of the -[Fe-pmd-Fe]$_\infty$- chains imposes the generation of such an unusual coordination network.

Crystal structure at 220 K: At 220 K, the average Fe−N bond lengths are still consistent with a HS state. However, the average Fe−N bond length for Fe(5) is appreciably shorter [2.08(5) Å] than for Fe(1)–(4) [2.17(4), 2.17(4), 2.15(4) and 2.16(5) Å, for Fe(1), Fe(2), Fe(3) and Fe(4), respectively]. This is in line with the ~4% LS state observed from the magnetic data at this temperature and is consistent with a change in volume between 290 K and 220 K of only around 0.4%.

The Fe–Fe distances within the -[Fe-pmd-Fe]$_\infty$- chains have shortened by an average of 0.022(2) Å with respect to their values at 290 K [Fe(1)···Fe(1) 6.1274(2) Å; Fe(2)···Fe(3) 6.155(1) Å, Fe(3)···Fe(2) 6.131(1) Å and Fe(4)···Fe(5) 6.1270(2) Å]. The shortest Ag···Ag contacts are still in the same range as at 290 K.

Crystal structure at 170 K: At 170 K, the system is situated half-way between the first and the second step of the spin transition (Figure 1). The change in the unit cell volume between the HS state (220 K) and the intermediate state (170 K) is around 3.3%, clearly indicating the presence of a HS $\rightleftarrows$ LS spin transition (Table 1). The variation of the unit cell volume associated with the first step has been evaluated as $\Delta V_1 = V(220 \text{ K})^* - V(170 \text{ K}) = 215$ Å^3, where $V(220 \text{ K})^*$ is the volume at 220 K corrected for the smooth spin change
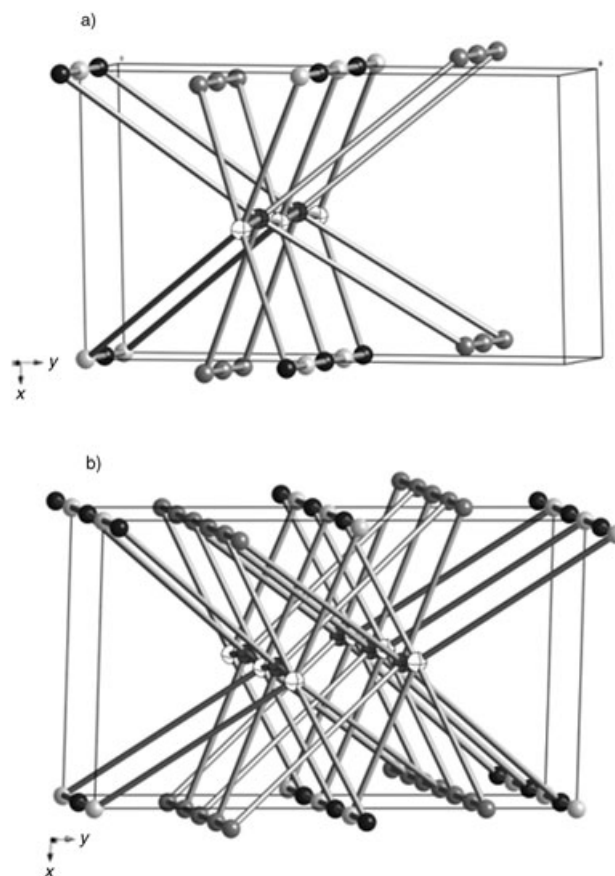

Figure 6. Schematic representations of the connectivity of a particular -[Fe(2)-pmd-Fe(3)]$_\infty$- chain with four -[Fe(1)-pmd-Fe(1)]$_\infty$- and -[Fe(4)-pmd-Fe(5)]$_\infty$- chains belonging to adjacent iron(II) layers a) and to a complete unit cell b), showing the (6,6) topology of the network and the interpenetration of the (6,6) circuits.

of ~4% (~30% of the Fe(5) ions) in the temperature range 290–220 K (see Supporting Information for more details). This corresponds to 26.9 Å^3 per spin changing complex in the high-temperature step. In addition, this change in the spin state is accompanied by a sharp change of the crystal's color from yellow to red.

The average Fe–N$_{av}$ bond lengths (Table 2) show that now only those bond lengths corresponding to Fe(2)−N and Fe(4)−N [2.16(5) and 2.15(3) Å, respectively] are consistent with a HS state. While those for Fe(3)−N and Fe(5)−N are consistent with a LS state [1.96(2) Å and 1.94(3) Å, respectively], the Fe(1)−N distance appears to be in an intermediate situation [2.04(3) Å]. The average change ΔR(Fe–N) on spin change, 0.2 Å, is consistent with a full HS-to-LS change for Fe(3)−N and Fe(5)−N while ΔR(Fe–N) = 0.11 Å for Fe(1)–N suggests a mixing of HS and LS states. In terms of volumes of the coordination octahedrons, those for Fe(2) and Fe(4) are 13.40 and 13.26 Å^3, those for Fe(3) and Fe(5) are 10.01 and 9.72 Å^3, while for Fe(1) there is an intermediate value of 11.33 Å^3; these values are in agreement with the rationalization above.

The Fe–Fe distances within the -[Fe-pmd-Fe]$_\infty$- chains have also shortened on average by a further 0.165(4) Å,

with respect to their values at 220 K [Fe(1)···Fe(1) 5.9637(3) Å, Fe(2)···Fe(3) 5.987(2) Å, Fe(3)···Fe(2) 5.966(2) Å and Fe(4)···Fe(5) 5.9633(3) Å]. The shortest Ag···Ag contacts now split in two groups, one around 2.97(1) Å and the other at 3.00(1) Å, the latter still in the same range as at 290 K (see Table 4).

The data reveal that an alternating arrangement exists of -[HS-LS-HS]$_\infty$- states in the two chains formed by two inequivalent iron atoms, namely -[Fe(2)-pmd-Fe(3)]$_\infty$- and -[Fe(4)-pmd-Fe(5)]$_\infty$-). Meanwhile, from the Fe–N distances and octahedral volume, it seems that only half of the Fe(1) atoms change spin state, as the diffraction technique only "sees" an average of these two states. In principle, if this change were produced in an orderly manner, a change of the symmetry should be observed in the diffraction data. However, any additional reflections that would arise from this change would be very weak. As the present diffraction data is not of sufficiently high quality, the apparent absence of additional reflections at the plateau temperature does not exclude long-range ordering and the formation of alternating -[HS-LS-HS]$_\infty$- Fe(1) chains. Indeed, a random distribution of half of these ions in different spin states within the crystal could produce strains which could lead to the destruction of the crystal itself, which was not observed. In addition, the formation of alternating high- and low-spin iron centers in the other chains supports the idea that ordering may be present in the Fe(1) chain.

It is worthwhile pointing out that only a few well-documented examples of two-step SCO transitions have been reported. The first of these examples is the mononuclear complex [Fe(2-pic)$_3$]Cl$_2$·EtOH (2-pic = 2-picolyl-amine).[20] For this compound, there is only one crystallographically distinct iron center in both the HS state and in the LS state.[21] The nature of the intermediate phase formed in the plateau has been revealed in a recent detailed structural study performed over a wide range of temperatures.[22] In contrast to previous studies,[23] this new structural analysis clearly establishes that long-range order occurs defining infinite -[LS-HS-LS]- chains of [Fe(2-pic)$_3$]$^{2+}$ molecules in the plateau. Within each chain, the molecules interact with each other strongly via hydrogen bonding through Cl$^-$ anions and EtOH solvent molecules. Using synchrotron radiation, Bürgi and co-workers found additional Bragg reflections that indicated the presence of a superstructure caused by the separation of the unique iron center into two and, consequently, a doubling of the unit cell size.[22] However, these reflections had not been observed for this compound during earlier experiments using laboratory X-ray sources.

A second relevant example of two-step SCO is provided by the monomeric compound {Fe[5-NO$_2$-sal-N(1,4,7,10)]}, where 5-NO$_2$-sal-N(1,4,7,10) is a hexadentate ligand synthesized from the condensation of 5-NO$_2$-salicylaldehyde with 1,4,7,10-tetraazadecane. For this compound the two-step conversion occurs in the same temperature range as two crystallographic phase transitions, which enables the identification of two equally distributed sets of molecules in the crystal.[24] Another case of interest here is that of

{Fe[HC(3,5-Me$_2$pz)$_3$]$_2$}(BF$_4$)$_2$ (where HC(3,5-Me$_2$pz)$_3$ = tris(3,5-dimethylpyrazolyl)methane), in which there is only one iron(II) site at room temperature, but following a crystallographic phase transition, two different sites, one in the LS state and the other in the HS state, appear in the middle of the plateau.[25]

Thermal and pressure induced step-wise transitions have also been observed in the binuclear compounds {Fe[L(NCX)$_2$]$_2$(bpym)} where bpym is 2,2'-bipyrimidine, X = S or Se and L = bpym or bt (bt = 2,2'-bi-2-thiazoline).[26] The crystal structure of {Fe[bt(NCS)$_2$]$_2$(bpym)} has been recently studied at different temperatures including the plateau where the iron(II) ions in each binuclear unit are expected to define non-centrosymmetric HS–LS spin pairs.[27a] In this compound the two-step character cannot be attributed to the existence of two crystallographically inequivalent iron(II) sites, as all the Fe atoms are equivalent in the whole range of temperatures. The occurrence of two steps was attributed to a synergistic effect between intramolecular interactions favoring HS–LS species and intermolecular interactions favoring HS–HS or LS–LS species. Studies on two new dimeric SCO iron(II) compounds {Fe[phdia(NCS)$_2$]$_2$(phdia)}[27b] (phdia = 4,7-phenantroline-5,6-diamine) and {[Fe(bt-pen)]$_2$[N(CN)$_2$]}(BF$_4$)$_3$[27c] (btpen = N,N',N'-tris(2-pyridylmethyl)ethylenedy-amine) give support to this statement.

Finally, the only polymeric system in which a two-step spin transition has been described is the 3D compound [Fe(btr)$_3$](ClO$_4$)$_2$ (btr = 4,4'-bis-1,2,4-triazole). In this particular case, the reason for the observation of the two steps is the occurrence of two crystallographically inequivalent iron(II) sites with slightly different ligand field strengths and, consequently, different values of ΔH and ΔS and critical temperatures.[28]

So, in these cases a variety of behavior has been seen, but these examples demonstrate that there is precedence for ordering and the examples like those discussed by Bürgi and co-workers show how an inability to find evidence of ordering may be due to limitations of the experiment rather than an absence of order.

Thus, despite the differences, a comparison deserves to be made between the title compound and the bpym-bridged iron(II) dinuclear compounds. In the dinuclear compounds the species that determine the occurrence of the plateau have been identified as distinct HS–LS spin pairs, by using a combination of Mössbauer spectroscopy in the presence of a magnetic field (5 T) and the LIESST effect at 4.2 K.[29] Similarly, the pmd bridged iron chains in the present work form alternating -[HS-LS-HS]$_\infty$- chains unequivocally for Fe(2)–Fe(3) and Fe(4)–Fe(5) atoms. Consequently, it is reasonable to think that the bridging ligand (bpym or pmd) plays an important role in the stabilization of the unlike-spin species in the plateau. Indeed, electronic communication between the iron(II) centers takes place through the bpym bridge, hence similar effects should be expected for the pmd bridge. For this reason and despite the lack of crystallographic evidence, we believe that there may be a HS–LS ordering in the Fe(1) chains at the plateau between the transitions.

Crystal structures at 90 and 30 K: At these temperatures the spin transition is complete, and the values of the reported structural parameters adjust accordingly. The change of the unit cell volume (Table 1) between the intermediate state (170 K) and the LS state (90 and 30 K) is around 4.1%, clearly indicating a further HS–LS spin transition and the crystal's color goes now from red to a darker red. The average Fe–N_{eq} and Fe–N_{ax} bond lengths of 1.96 Å for all iron centers (Table 2) are now consistent with an overall LS state as observed from the magnetic data. As above, the unit cell volume difference due to the spin transition for the second, low-temperature step $\Delta V_2 = V(170 \text{ K}) - V(90 \text{ K}) = 250.6 \text{ Å}^3$ or 31.3 Å^3 per spin changing center.

The Fe–Fe distances within the -[Fe-pmd-Fe]$_\infty$- chains have shortened now by an average of 0.173(4) Å with respect to their values at 170 K [Fe(1)···Fe(1) 5.7935(3) Å, Fe(2)···Fe(3) 5.812(2) Å, Fe(3)···Fe(2) 5.7887(2) Å and Fe(4)···Fe(5) 5.7919(3) Å]. The shortest Ag···Ag contacts are again back in one group at around 2.94(1) Å (see Table 4).

Crystal structure at 30 K after irradiation with light: The change of the unit cell volume (see Table 1) between the LS state (30 K) and the light induced HS state (30 K) is around 7.4%, clearly suggesting a substantial LS to HS spin conversion. In addition, the crystal color goes from red back to yellow. As seen in Table 2, the average Fe–N_{eq} and Fe–N_{ax} bond lengths for Fe(1) to Fe(4) are consistent with a HS state, as observed from the magnetic data. The values for Fe(5), however, are consistent with a LS state. Fe(5) represents 12.5% of the total iron centers in the unit cell. We have already noted that Fe(5) is more prone to adopt the LS state than Fe(1) to Fe(4) and as we have indicated above, ~30% of Fe(5) is in the LS spin state at 220 K (~4% of the total Fe content). Thus, Fe(5) must have a larger energy difference between the HS and LS potential energy wells and, consequently, a lower HS→LS activation energy barrier than the rest of the other iron atoms. A similar reasoning may be applied to $^1/_2$Fe(1) and Fe(3) with respect to the other iron atoms [$^1/_2$Fe(1), Fe(2) and Fe(4)] as the former set of iron atoms are the next to change their spin state, as shown by the structural data at 170 K.

Thus at 30 K 87.5% of the spin centers possess a lifetime of the light-induced HS state as long as required for the crystallographic measurements carried out in this case. Upon irradiation the unit cell volume was found to have increased by 460 Å^3, corresponding to 32.9 Å^3 per spin changing center.

The Fe–Fe distances within the -[Fe-pmd-Fe]$_\infty$- chains have increased by an average of 0.319(5) Å with respect to their values at 30 K before irradiation and differ from their values at 290 K by only 0.057(2) Å [Fe(1)···Fe(1) 6.092(1) Å, Fe(2)···Fe(3) 6.116(5) Å, Fe(3)···Fe(2) 6.100(5) Å and Fe(4)···Fe(5) 6.091(1) Å]. The shortest Ag···Ag contacts are back in the range 2.98–3.02 Å, almost the same range as at 290 K (Table 4).

Differential scanning calorimetry (DSC) measurements: The calorimetric measurements were carried out in the 300–120 K temperature range. A smooth line was interpolated from the values in the normal regions. The heat capacity due to the transition was deduced by subtraction of this baseline. The temperature dependence of the anomalous heat capacity, Δc_p, in the warming mode is shown in Figure 7. The Δc_p versus T curve shows the occurrence of
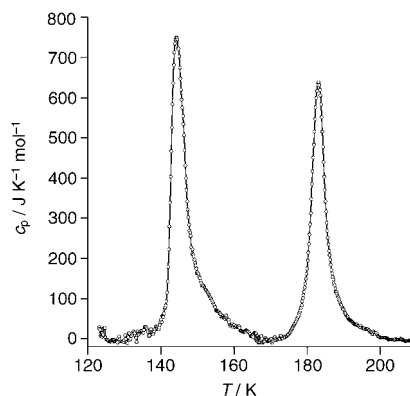

Figure 7. Differential scanning calorimetric measurement of the title compound with the normal lattice contribution subtracted.

two asymmetric peaks, one for each step, at $T_{c1} = 185.2$ and at $T_{c2} = 147.7$ K. These values agree well with those observed from the $\chi_M T$ versus T plot in the heating mode. The overall enthalpy (ΔH) and entropy (ΔS) variations associated with each step determined from the DSC curves are, $\Delta H_1 = 3.6 \pm 0.4 \text{ kJ mol}^{-1}$, $\Delta H_2 = 4.8 \pm 0.4 \text{ kJ mol}^{-1}$ and $\Delta S_1 = 19.5 \pm 3 \text{ J K}^{-1} \text{mol}^{-1}$, $\Delta S_2 = 33.5 \pm 3 \text{ J K}^{-1} \text{mol}^{-1}$. The overall variations $\Delta H = 8.4 \text{ kJ mol}^{-1}$ and $\Delta S = 53 \text{ J K}^{-1} \text{mol}^{-1}$ are within the experimental range generally observed for iron(II) SCO compounds.[30] It is worth noting that a symmetric distribution of ΔS between the two steps should be expected. However, ΔS_1 is significantly smaller than ΔS_2. This fact is most probably related to the different unit cell volume variations associated with the two steps: $\Delta V_1 = 215$ and $\Delta V_2 = 250.6 \text{ Å}^3$ for the first and the second step, respectively. As $\Delta V_2 > \Delta V_1$, the contribution of low frequency phonons to the entropy change is expected to be larger for the second step.

Closely related to these facts are the changes observed in the intermetallic Ag···Ag distances upon SCO. The most significant variations range between 0.040 Å, [Ag(8)···Ag(9)], and 0.180 Å [Ag(10)···Ag(11)], in the temperature interval 290–90 K. When comparing the variations of the Ag···Ag distances occurring in each thermally induced step (first step is 170–290 K and second step is 90–170 K), it becomes apparent that only 37.5% of the total variation takes place in the first step. This is probably the reason why the title compound displays an asymmetric variation in the unit cell volume and, consequently, in ΔS and Δc_p. In addition, the structure at 30 K after irradiation also shows significant changes in the Ag···Ag distances stemming exclusively from the spin change (see Table 4). These results support the occurrence of a synergy between SCO and metallophilic interactions and as such are only the second example where this

has been seen (the first was recently observed in the compound {Fe(3-cyanopyridine)$_2$[Ag(CN)$_2$]$_2$}·^{2}/$_3$H$_2$O, which is made up of triple interpenetration of an expanded version of the NbO structure).[7d]

Visible absorption spectroscopy: Figure 8a and b display the single crystal absorption spectra obtained during the thermal transition for descending and ascending temperatures, respectively. As the temperature is lowered a band grows in intensity with a maximum at ~525 nm. At the same time there is an important increase in intensity below 500 nm, so that the 525 nm band appears only as a shoulder on the tail of the intense high-energy transition. Whereas this high-energy transition can be attributed to a metal-ligand charge transfer (MLCT) transition, the intensity of the band at 525 nm is in line with a d–d transition of the low spin state, more precisely with the spin-allowed $^1A_1 \rightarrow {}^1T_1$ transition. Already qualitatively there is a clear indication of a step-wise transition. The molar fraction of iron(II) centers in the high-spin state, γ_{HS}, can be determined from the relative integrated intensity of the characteristic LS absorption between 500 and 650 nm. The corresponding two-step thermal spin transition curve is presented in Figure 9. It closely resembles the $\chi_M T$ curve of Figure 1. In particular, the critical temperature for the high temperature step, $T_{c1} = 185$ K is identical. The lower temperature step is accompanied by a small hysteresis, with descending and ascending critical temperatures $T_{c2}\downarrow$ and $T_{c2}\uparrow$ of 147.5 and 150.0 K, respectively. At 2.5 K, the hysteresis is slightly larger than in the corresponding magnetic measurements and the curves are somewhat more abrupt. The key difference between the magnetic and the optical measurements is that the latter were performed on one single crystal, whereas for the former, a collection of micro-crystals with a certain size distribution were used. This is reflected in the apparently less abrupt transition observed in the magnetic measurements.

Even though according to the crystallographic measurements the spin transition for Fe(5) begins at a slightly higher temperature than for all the other iron centers, the five iron centers can thermodynamically be broken down into two sets: the first set contains Fe(3), Fe(5) and half of the Fe(1) atoms, which undergo the SCO transition during the high temperature step; the second set contains Fe(2), Fe(4) and the other half of Fe(1), which undergo the SCO transition during the low temperature step. Each set thus contains the same number of centers. In order to simulate the thermal spin transition, a simple model, which implies the presence of just two different sets of iron centers, was considered. The variation of the Gibbs free energy for the two sets can be written as Equation (1):

$$\Delta G_1 = \Delta H_1(\gamma_{HS1}, \gamma_{HS2}) - T\Delta S_1 \tag{1a}$$

$$\Delta G_2 = \Delta H_2(\gamma_{HS1}, \gamma_{HS2}) - T\Delta S_2 \tag{1b}$$

where $\Delta H_{1,2}$ are the enthalpy variations, and $\Delta S_{1,2}$ are the entropy variations for the two sets. γ_{HS1} and γ_{HS2} are high
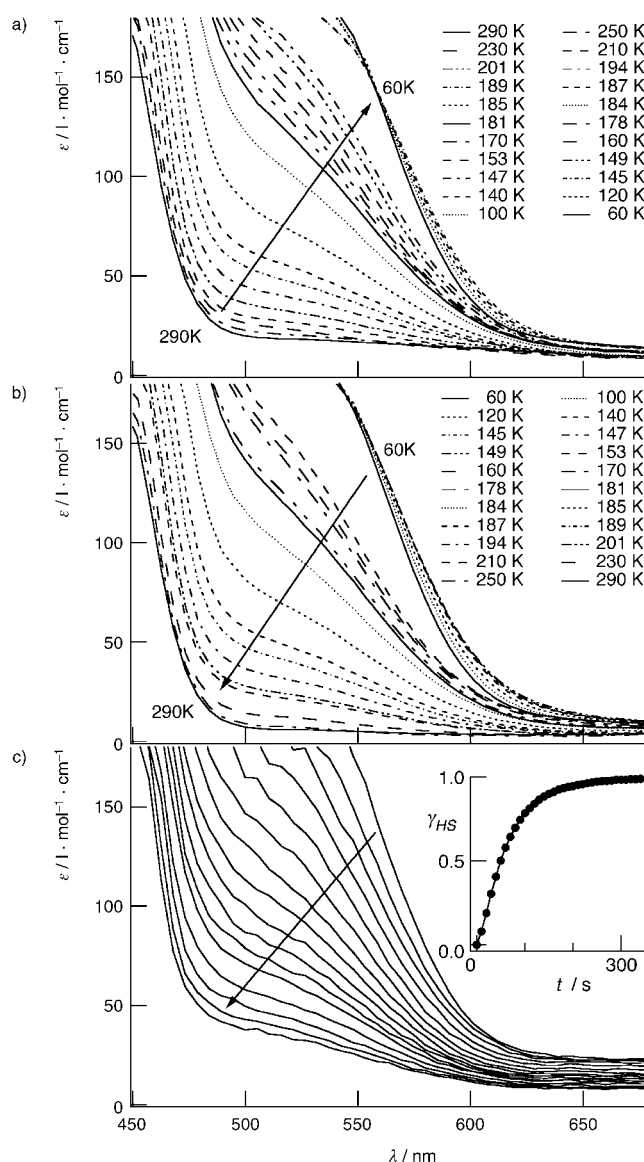

Figure 8. Single crystal absorption spectra of the title compound obtained for a) descending and b) ascending temperatures, and c) during photoexcitation at 10 K with 647 nm light, light-intensity 11 mW mm^{-2}, spectra recorded in intervals of 20 s. Inset: corresponding excitation curve.
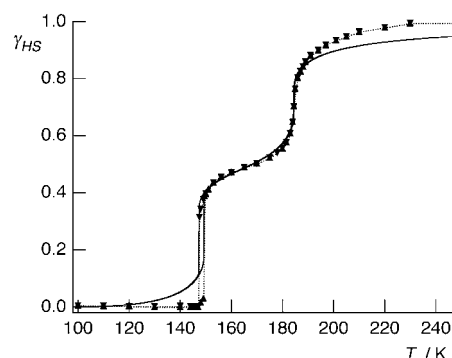

Figure 9. Thermal spin transition curve for the title compound as obtained from optical measurements. Experimental data (▼ descending temperature, ▲ ascending temperature) and simulation (——) as described in the text.

spin fractions for each step and both taken to go from 0 to 1, and the total high spin fraction $\gamma_{HS} = (\gamma_{HS1} + \gamma_{HS2})/2$. ΔS_1 and ΔS_2 can directly be identified with the entropy variations associated with the two steps obtained by the calorimetric measurements according to Equation (2):

$$\Delta S_1 = 2\Delta S_1^{exp} = 38.0\,\mathrm{J\,K^{-1}\,mol^{-1}} \tag{2a}$$

and

$$\Delta S_2 = 2\Delta S_2^{exp} = 67.0\,\mathrm{J\,K^{-1}\,mol^{-1}} \tag{2b}$$

For the enthalpy variation this is not the case. As a result of cooperative effects of elastic origin, ΔH_1 and ΔH_2 are functions of the HS fractions on both sets, γ_{HS1} and γ_{HS2}. The values determined from the calorimetric measurements correspond to the value at the transition temperature of each partial transition according to Equation (3):

$$\Delta H_1(\gamma_{HS1} = \tfrac{1}{2}, \gamma_{HS2} = 1) = \Delta H_1^0 = 2\Delta H_1^{exp} = 7.2\,\mathrm{kJ\,mol^{-1}} \tag{3a}$$

$$\Delta H_2(\gamma_{HS1} = 0, \gamma_{HS2} = \tfrac{1}{2}) = \Delta H_2^0 = 2\Delta H_2^{exp} = 9.6\,\mathrm{kJ\,mol^{-1}} \tag{3b}$$

In mean-field approximation ΔH_1 and ΔH_2 as functions of the high-spin fractions in the two sets can be expressed as follows:[31]

$$\Delta H_1(\gamma_{HS1}, \gamma_{HS2}) = \Delta H_1^0 - 2\Gamma_{11}(\gamma_{HS1} - \tfrac{1}{2}) - 2\Gamma_{12}(\gamma_{HS2} - 1) \tag{4a}$$

$$\Delta H_2(\gamma_{HS1}, \gamma_{HS2}) = \Delta H_2^0 - 2\Gamma_{22}(\gamma_{HS2} - \tfrac{1}{2}) - 2\Gamma_{21}\gamma_{HS1} \tag{4b}$$

where Γ_{11} and Γ_{22} are the interaction constants for the interaction within the two sets and Γ_{12} and Γ_{21} are the interaction constants between the two sets. Whereas the former are always positive, that is favoring the majority species in a "ferromagnetic-like" fashion, the latter can have either sign. From these expressions the following system of coupled equations can be obtained by Equation (5):

$$\frac{\gamma_{HS1}}{1-\gamma_{HS1}} = \exp\left(-\frac{\Delta H_1^0 - T\Delta S_1 - 2\Gamma_{11}(\gamma_{HS1} - \tfrac{1}{2}) - 2\Gamma_{12}(\gamma_{HS2} - 1)}{k_B T}\right) \tag{5a}$$

$$\frac{\gamma_{HS2}}{1-\gamma_{HS2}} = \exp\left(-\frac{\Delta H_2^0 - T\Delta S_2 - 2\Gamma_{22}(\gamma_{HS2} - \tfrac{1}{2}) - 2\Gamma_{21}\gamma_{HS1}}{k_B T}\right) \tag{5b}$$

This system of coupled equations can be solved numerically for any set of parameters. In order to reduce the number of parameters taken into account in the simulations, $\Gamma_{12} = \Gamma_{21}$ is assumed. The numerical solution obtained by using the above values for ΔH_1^0, ΔH_2^0, ΔS_1, and ΔS_2 and by optimizing Γ_{11} and Γ_{22} are presented in Figure 9, together with the ex-

perimental data. Because of the large difference in the critical temperatures of the two steps, the simulations are insensitive to the value of Γ_{12}, that is, to the interaction constant between the sets. The step is basically due to the two different values of ΔH^0 for the two sets of centers. With values of 2.8 kJ mol^{-1} and 3.1 kJ mol^{-1} for Γ_{11} and Γ_{22}, respectively, the interaction constants within each set are quite large. While they are not quite large enough to produce a hysteresis in the first step at 185 K they produce a small hysteresis for the second step at 148 K. The discrepancy between the calculated and the experimental curves at high temperatures results because the model with just two sets of centers is too crude. The fact that the experimental curves for the first step are much steeper than predicted by the simple model indicates that Γ_{12} and Γ_{21} are not zero. Although it is not possible to quantify them, the interactions between the two sets of centers are thought to be responsible for the splitting of the Fe(1) centers into the two sets, and therefore are of an "antiferromagnetic-like" nature.

LIESST effect and relaxation of the light-induced HS state: Figure 8c shows the bleaching of the band at 525 nm upon irradiation at 10 K with 647 nm light from a Kr$^+$ laser. Even though this wavelength is in the low energy tail of the intense low spin band, the light induced conversion to the HS state is quite efficient (see inset Figure 8c). A rough estimate indicates a quantum efficiency of at least 50%. The complete bleaching of the absorption band signifies that in the thin single crystal the light-induced conversion to the HS state occurs quantitatively at 10 K. Relaxation of the light induced HS state was followed both by magnetic susceptibility measurements as well as by absorption spectroscopy.

Figure 10 shows HS→LS relaxation curves in the dark using the latter technique for temperatures between 15 and 55 K. At the lowest temperature, a fraction of between 5 and 10% of all iron centers relaxes comparatively rapidly, that is within less than 3 h. In accordance with the structural results at 290, 220, 170 and particularly at 30 K after irradiation, this fraction has to be attributed to Fe(5), which has the largest driving force for the relaxation back to the LS state at low temperatures. At 15 K, around 12.5% of iron centers relax in 20 h. This amount coincides with the percentage of Fe(5) in the unit cell. The remaining iron centers do not noticeably relax back to the LS state within the same period. At 25 K a total fraction of about 40% relax to the LS state within 15 h. Thus, in addition to the 12.5% of Fe(5) centers another 27.5% relax at this temperature within this time. The crystallographic data recorded at 170 K indicate that the most destabilized HS atoms apart from Fe(5), are the $\tfrac{1}{2}$Fe(1) and Fe(3) centers (see Table 2), which all belong to the set of iron atoms undergoing the SCO transition during the first, high temperature step in the thermal transition. No clear evidence for the spin state relaxation of the $\tfrac{1}{2}$Fe(1)–Fe(3) subgroup from the crystallographic data at 30 K, after irradiation, was observed.
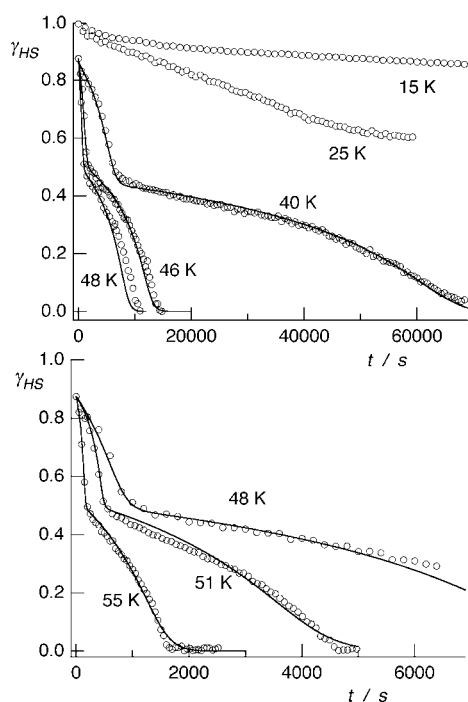
Figure 10. HS→LS relaxation curves recorded at different temperatures from optical measurements following quantitative photoexcitation at 10 K. Experimental data (○) and simulations (——).

At somewhat more elevated temperatures, that is between 40 and 55 K, all iron centers relax to the LS state within less than 20 h. In accordance with the thermal spin transition they do so in two steps. Both steps show the typical sigmoidal self-accelerated shape due to the cooperative effects.[23] The experimental curves at these elevated temperatures actually start at a total HS fraction of 85–90%, because Fe(5) decays on a much faster time scale at higher temperatures. Following the spirit of the treatment of the thermal spin transition and ignoring the finer details, the iron centers can again be grouped into two sets. As before, set 2 comprises Fe(2), Fe(4) and half of Fe(1) and set 1 comprises Fe(3) and the other half of Fe(1). Fe(5) is left out because of its faster relaxation at these temperatures. In a mean-field approximation the relaxation rate constants for the two sets at a given temperature depend upon the LS fraction according to:[23]

$$\frac{d\gamma_{HS1}}{dt} = -k_{HL1}^0 \, e^{(\alpha_{11}\gamma_{LS1} + \alpha_{12}\gamma_{LS2})} \gamma_{HS1} \tag{6a}$$

$$\frac{d\gamma_{HS2}}{dt} = -k_{HL2}^0 \, e^{(\alpha_{21}\gamma_{LS1} + \alpha_{22}\gamma_{LS2})} \gamma_{HS2} \tag{6b}$$

with γ_{HS1} and γ_{HS2} both going from 1 at the beginning of the relaxation to 0 at the end. The total HS fraction is given by $\gamma_{HS} = (^3/_4\gamma_{HS1} + \gamma_{HS2})/2$. k_{HL1}^0 and k_{HL2}^0 are the relaxation rate constants at a nominal total HS fraction of $^7/_8$, that is at the beginning of the relaxation curves, and α_{11} and α_{22} are the cooperativity parameters describing the self-accelera-

tion. As for the interaction parameters Γ_{12} and Γ_{21}, α_{12} and α_{21} describe the interaction between the two sets. Since the two sets of iron centers relax on different time scales, it is not possible to actually extract α_{12} and α_{21} from the experimental data. So, during the first step in the relaxation curve, γ_{LS2} remains virtually zero, during the second step γ_{LS1} has essentially reached a value of 1. Thus, with $\gamma_{LSi} = 1 - \gamma_{HSi}$, Equation (6) can be recast:

$$\frac{d\gamma_{HS1}}{dt} \approx -k_{HL1}^0{}' \, e^{(\alpha_{11}(1-\gamma_{HS1}))} \gamma_{HS1} \tag{7a}$$

$$\frac{d\gamma_{HS2}}{dt} \approx -k_{HL2}^0{}' \, e^{(\alpha_{22}(1-\gamma_{HS2}))} \gamma_{HS2} \tag{7b}$$

This pair of differential equations can be solved numerically. The best fit values for α_{11} and α_{22} together with $k_{HL1}^0{}'$ and $k_{HL2}^0{}'$ are given in Table 5. The corresponding calculated relaxation curves are included in Figure 10. In mean-field approximation and in the thermally activated region the acceleration factor $\alpha \approx \Gamma/k_B T$.[23] Thus, as expected, α_{11} and α_{22} both decrease with increasing temperature and α_{11} is somewhat smaller than α_{22}. However, the absolute values of the acceleration parameters are substantially smaller than $\Gamma/k_B T$. There are several reasons for this: a) 40 to 50 K is not fully in the thermally activated region, b) there is a comparatively large inhomogeneous distribution of the zero-point energy difference and c) the specific nearest neighbor interactions of the "antiferromagnetic" type influence the relaxation behavior. Unfortunately, it is not possible to differentiate between the three unambiguously. However, the fact that the crystallographically equivalent Fe(1) centers are again shared by the two sets supports the previous conclusion that nearest neighbor interactions of an "antiferromagnetic-like" type must be present.

Table 5. Parameter values obtained from simulation of the two relaxation steps: α_{11} and α_{22} account for cooperativity, $k_{HL1}^0{}'$ and $k_{HL2}^0{}'$ are the initial rate constants.

T [K]	α_{11}	α_{22}	$k_{HL1}^0{}'/s^{-1}$	$k_{HL2}^0{}'/s^{-1}$
40	3.0	4.1	7.5×10^{-5}	5.5×10^{-6}
46	2.6	3.9	3.6×10^{-4}	2.9×10^{-5}
48	2.4	3.75	6.5×10^{-4}	4.4×10^{-5}
51	2.2	3.4	1.1×10^{-3}	1.1×10^{-4}
55	2.1	3.2	4.9×10^{-3}	3.0×10^{-4}

Light induced thermal hysteresis: Some years ago, Desaix et al.[32] and Létard et al.[33] showed that continuous photoexcitation can maintain a considerable fraction of the iron centers in the high spin state at temperatures where normally the relaxation is already quite fast. This photoexcitation together with the cooperative relaxation leads to the so-called Light Induced Thermal Hysteresis (LITH),[32,33] where a fraction of the complexes is maintained in the HS state in a pseudo steady-state under continuous irradiation while the temperature is slowly scanned typically from 10 up to

around 80 K and back again. A corresponding LITH cycle for the title compound, shown in Figure 11, was recorded at a constant temperature scan rate of 4 K per hour, by using
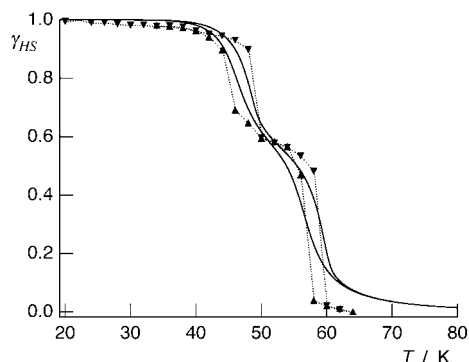

Figure 11. Light-induced thermal hysteresis (LITH): experimental data (▼ descending temperature, ▲ ascending temperature) and simulations (——) as described in the text. The parameter values used for the simulated curves were α_{11}, α_{22} (given in Table 5) and $I\sigma = 0.002$ s^{-1}.

the 647 nm line of a Kr$^+$ laser with an intensity at the sample of 4 mW mm^{-2}. As for the thermal spin-transition, the LITH cycle shows two steps. The set of iron centers belonging to the low temperature step in the LITH cycle corresponds to the faster relaxing centers in the relaxation curves of Figure 10 and therefore they belong to the set of the high-temperature step of the thermal spin transition. The second step in the LITH curve corresponds to the centers, which relax slower and therefore belong to the low-temperature step in the thermal transition curve.

The LITH cycle can be simulated by using the following system of coupled differential equations with the terms $(1 - \gamma_{HSi})I\sigma$ added to account for the photoexcitation:

$$\frac{d\gamma_{HS1}}{dt} = (1 - \gamma_{HS1})I\sigma - k_{HL1}^{0\,\prime}(T)\,\gamma_{HS1}\,e^{(\alpha_{11}(T)(1 - \gamma_{HS1}))} \qquad (8a)$$

$$\frac{d\gamma_{HS2}}{dt} = (1 - \gamma_{HS2})I\sigma - k_{HL2}^{0\,\prime}(T)\gamma_{HS2}\,e^{(\alpha_{22}(T)(1 - \gamma_{HS2}))} \qquad (8b)$$

where I is the radiation intensity, and σ is the absorption cross section at the irradiation wavelength of 647 nm. The numerical solution of these equations was performed by using the parameters for α_{11}, α_{22}, $k_{HL1}^{0\,\prime}$ and $k_{HL2}^{0\,\prime}$ as a function of T taken from Table 5, and by setting the temperature scan speed to the experimental speed of 4 K h^{-1} and $I\sigma = 0.002$ s^{-1}. The calculated curves for the up and down temperature scans are included in Figure 11. The agreement between calculated and experimental curves is satisfactory. The fact that the hystereses are steeper in the experimental curves than in the simulations indicates that the mean-field treatment has its limitations.

Concluding Remarks

In this paper we have described the synthesis, structure and physical properties of a new coordination polymer, which presents an unprecedented (6,6)-network topology. This polymer is a singular material as there are five crystallographically distinct iron(II) sites. These sites display small differences in the axially distorted [FeN$_6$] coordination octahedrons interlinked by three different bridging ligands namely pmd, [Ag(CN)$_2$]$^-$ and [Ag$_2$(CN)$_3$]$^-$. These three different ligands impose vastly different iron-to-iron separations due to the different lengths of the bridges: 6.2, 10.15 and 15.6 Å, respectively. The iron(II) sites are distinguished via the number and distribution of the [Ag(CN)$_2$]$^-$ and [Ag$_2$(CN)$_3$]$^-$ ligands that define the equatorial plane of the octahedrons, as well as the different connectivity between iron sites through these bridges. The silver–cyanide system of bridges connects all the iron(II) atoms together leading to an intricate 3D network {Fe[Ag(CN)$_2$][Ag$_2$(CN)$_3$]}$_\infty$. Such amazing coordination at each site imposed by the coordination topology of the bridging pmd ligands determines the occurrence of self-interpenetration of the (6,6) {(Fe-pmd-Fe-pmd-Fe)$_2$-L$_2$, where L = [Ag(CN)$_2$]$^-$ or [Ag$_2$(CN)$_3$]$^-$} circuits. As far as we are aware, no example of such a network has been reported to date and this coupled with the occurrence of strong argentophilic interactions within the network, make the title structure truly remarkable.

Magnetic susceptibility measurements reflect the occurrence of a two-step spin transition involving each step ca. 50% of the iron(II) sites. This process is accompanied by a drastic color change from yellow (HS) to deep red (LS). Taking advantage of this color change, the two-step transition has also been monitored using single-crystal electronic spectroscopic studies in the visible region. The results from the bulk magnetic studies and single-crystal optical studies match well. The thermodynamic parameters associated with the two-step transition have been calculated from the anomalous heat capacity, c_p, of the title compound. As expected, a graph depicting c_p versus T is characterized by two maxima centered at around $T_{c1} = 185$ K and $T_{c2} = 148$ K, respectively. However, the maxima display significantly different values of c_p and, consequently, different entropic contributions for each step. ΔS_1 (for the high temperature transition) is noticeably smaller than ΔS_2.

Diffraction studies show a similar structural behavior on cooling, with two steps clearly visible. Data collected at the intermediate plateau reveal that only half of the iron centers are LS, arranged in chains of alternating -LS-HS-LS-HS-centers. In the same way, argentophilic interactions are found to follow a stepwise change, with about 40% of the total change observed taking place in the high temperature step. The unit cell volume variation is also noticeably smaller than that of the second, low temperature step, establishing a direct link between both events and the change in entropy. Synergy between metallophilic interactions and the SCO phenomenon has already been reported in previous

work, however, this is the first time in which its effects have been thermodynamically quantified.

Photomagnetic and photooptical studies show that the compound undergoes LIESST at low temperature. Relaxation of the sample at different temperatures (Figure 10) shows that the iron atoms in the lattice can be divided into two groups from the point of view of the magnetic and optical behavior, in agreement with the diffraction results. Related to the two steps in the thermal transition curve, there are two distinctly different slopes seen in the relaxation curves and the first section of the relaxation is faster than the second section.

Structural studies have led to the identification of the first iron center (Fe(5)) to undergo thermal spin crossover. Similar studies carried out at 30 K on the photoexcited state show that Fe(5) is in the LS state, the others remain trapped at the HS state. Thus the Fe(5) center appears to show the lowest activation barrier for the relaxation HS-to-LS and due to the nature of the diffraction experiment relaxes too fast to be measured at 30 K.

A full thermodynamic and kinetic analysis of the spin transitions has been possible from the direct observation of the thermal- and light-induced structural changes associated to each iron(II) site, which have revealed for the first time the microscopic mechanism of a complex cooperative spin transition in a fascinating material.

Experimental Section

Materials: Fe(BF$_4$)$_2$·6H$_2$O, K[Ag(CN)$_2$] and pmd were purchased from commercial sources and used as received.

Preparation: The material was synthesized by slow diffusion, under an argon atmosphere, of two aqueous solutions containing stoichiometric amounts of Fe(BF$_4$)$_2$·6H$_2$O (0.185 mmol, 2 mL)/pyrimidine (0.374 mmol, 2 mL) in one side and K[Ag(CN)$_2$] (0.374 mmol, 2 mL) in the other side of an H-shaped vessel. Over the following three weeks stable pale-yellow prismatic crystals of {Fe(pmd)(H$_2$O)[Ag(CN)$_2$]$_2$}·H$_2$O (yield ca. 50%)[9] were formed, together with well defined clumps of flattened yellow needles of {Fe(pmd)[Ag(CN)$_2$][Ag$_2$(CN)$_3$]} (yield ca. 10%). The crystals have a quite different texture and aspect making it easy to separate them by hand. However, systematic separation of the two compounds was performed with the aid of a binocular lens in order to avoid any contamination of the massive samples used for magnetic and calorimetric experiments. Elemental analysis calcd (%) for C$_9$H$_4$N$_7$Ag$_3$Fe: C 18.33, H 0.68, N 16.63; found: C 18.52, H 0.73, N 16.49.

Magnetic and photomagnetic measurements: The variable temperature magnetic susceptibility measurements were carried out by using samples (20–30 mg) consisting of small needles of the title compound, using a Quantum Design MPMS2 SQUID susceptometer equipped with a 5.5 T magnet, operating at 1 T and at temperatures from 300–1.8 K. The susceptometer was calibrated with (NH$_4$)$_2$Mn(SO$_4$)$_2$·12H$_2$O. Photomagnetic experiments were carried out using a Xe lamp with a 350–800 nm filter system coupled through an optical fiber to the sample chamber of the SQUID susceptometer; the power output was 2 mWcm^{-2}. Experimental susceptibilities were corrected for diamagnetism of the constituent atoms by the use of Pascal's constants.

X-ray single crystal diffraction: Single crystal X-ray diffraction experiments were carried out at 290, 220, 170, and 90 K, by using graphite-monochromated Mo$_{K\alpha}$ radiation ($\lambda = 0.71073$ Å) on a Bruker SMART-CCD 6000 area detector diffractometer equipped with an Oxford Cryostream N$_2$ open-flow cooling device.[34] Series of narrow ω scans (0.3°) were per-

formed at several settings in such a way as to cover a sphere of reciprocal space to a maximum resolution of 0.75 Å. Further datasets were collected from the same crystal, at 30 K and at 30 K after irradiating the crystal with a He/Ne laser for 2 h, by using graphite-monochromated Mo$_{K\alpha}$ radiation ($\lambda = 0.71073$ Å) on a Bruker SMART-1 K CCD area detector diffractometer equipped with an Oxford Cryosystems Helix He open-flow cryostat.[35] The 10 mW 633 nm laser beam was directed onto the crystal by a combination of mirrors and prisms.[36]

Unfortunately all crystals tried to date have been found to be non-merohedral twins and the crystal used for the diffraction experiments described herein is no exception. Cell parameters and corresponding orientation matrices for the two components of the twin were determined separately and refined by using the SMART software.[37] The relationship between the components can be described with the matrix:

$$\begin{pmatrix} -1.00 & 0.00 & -0.37 \\ 0.00 & -1.00 & 0.00 \\ 0.00 & 0.00 & 1.00 \end{pmatrix}$$

which approximately corresponds to a 180° rotation about the c axis. Integration of the raw intensity data for both components was carried out using SAINT V6.45 A.[38] An absorption correction was performed and reflections merged by using TWINABS V1.05.[39]

The structure was solved by direct methods using rough intensities derived from the major twin component. The final refinements at each temperature (including refinement of the twin ratio) were carried out by full-matrix least squares on F^2 (with SHELXTL),[40] using only reflections containing a contribution from the major component. Crystal data are listed in Table 1.

Iron and silver atoms were refined with anisotropic displacement parameters, but due to difficulties caused by the twinning, carbon and nitrogen atoms were refined isotropically at all temperatures. In addition, the 30 K structure (prior to irradiation) was refined with several constraints on the Ag, C and N thermal displacement parameters. Hydrogen atoms were positioned geometrically and refined using a riding model.

Differential scanning calorimetry (DSC): Calorimetric measurements were performed using a differential scanning calorimeter Mettler Toledo DSC 821^e. Low temperatures were obtained with an aluminium block attached to the sample holder, refrigerated with a flow of liquid nitrogen and stabilized at a temperature of 110 K. The sample holder was kept in a dry box under a flow of dry nitrogen gas to avoid water condensation. The measurements were carried out using around 20 mg of powdered sample sealed in aluminium pans with a mechanical crimp. Temperature and heat flow calibrations were made with standard samples of indium by using its melting transition (429.6 K, 28.45 Jg^{-1}). An overall accuracy of ±0.2 K in temperature and ±2% in the heat capacity is estimated. The uncertainty increases for the determination of the anomalous enthalpy and entropy due to the subtraction of an unknown baseline.

Visible absorption single crystal spectroscopy: A copper sample holder, with a single crystal of 21 μm thickness mounted to cover an aperture of ca. 0.2 mm diameter, was inserted into a closed cycle cryostat (Oxford Instruments CCC1100T) capable of reaching 11 K with the sample sitting in helium exchange gas for efficient cooling. Full absorption spectra were recorded between 450 and 750 nm by using a home built spectrometer equipped with a CCD camera and light from a 50 W tungsten halogen source. The light level from the lamp was kept well bellow the threshold for any noticeable light-induced spin state conversion.

Acknowledgement

[1] a) H. A. Goodwin, *Coord. Chem. Rev.* **1976**, *18*, 293–325; b) P. Gütlich, *Struct. Bonding (Berlin)* **1981**, *44*, 83–195; c) E. König, *Struct. Bonding (Berlin)* **1991**, *76*, 51–152; d) E. König, G. Ritter, S. K. Kulshreshtha, *Chem. Rev.* **1985**, *85*, 219–234; e) P. Gütlich, A. Hauser, H. Spiering, *Angew. Chem.* **1994**, *106*, 2109–2139; *Angew. Chem. Int. Ed. Engl.* **1994**, *33*, 2024–2054.

[2] a) K. R. Dunbar, R. A. Heintz, *Prog. Inorg. Chem.* **1997**, *45*, 283–391; b) M. Verdaguer, A. Bleuzen, V. Marvaud, J. Vaissermann, G. M. Seuleiman, C. Desplanches, A. Scuiller, C. Train, R. Garde, G. Gelly, C. Lomenech, I. Rosenman, P. Veillet, C. Cartier, F. Villain, *Coord. Chem. Rev.* **1999**, *190–192*, 1023–1047; c) M. Ohba, H. Okawa, *Coord. Chem. Rev.* **2000**, *198*, 313–328.

[3] T. Iwamoto, *Inclusion Compounds. Vol. 5* (Eds.: J. L. Atwood, J. E. D. Davies, D. D. MacNicol), Oxford University Press, London (UK), **1991**, pp. 177.

[4] T. Kitazawa, Y. Gomi, M. Takahashi, M. Takeda, A. Enemoto, T. Miyazaki, T. Enoki, *J. Mater. Chem.* **1996**, *6*, 119–121.

[5] V. Niel, J. M. Martinez-Agudo, M. C. Muñoz, A. B. Gaspar, J. A. Real, *Inorg. Chem.* **2001**, *40*, 3838–3839.

[6] G. Molnár, V. Niel, J. A. Real, L. Dubrovinsky, A. Bousseksou, J. J. McGarvey, *J. Phys. Chem. B* **2003**, *107*, 3149–3155.

[7] a) V. Niel, M. C. Muñoz, A. B. Gaspar, A. Galet, G. Levchenko, J. A. Real, *Chem. Eur. J.* **2002**, *8*, 2446–2453; b) V. Niel, A. Galet, A. B. Gaspar, M. C. Muñoz, J. A. Real, *Chem. Commun.* **2003**, 1248–1249; c) V. Niel, A. L. Thompson, M. C. Muñoz, A. Galet, A. E. Goeta, J. A. Real, *Angew. Chem.* **2003**, *115*, 3890–3893; *Angew. Chem. Int. Ed.* **2003**, *42*, 3759–3763; d) A. Galet, V. Niel, M. C. Muñoz, J. A. Real, *J. Am. Chem. Soc.* **2003**, *125*, 14224–14225.

[8] V. Niel, PhD. Thesis, Universitat de València (Spain), **2002**.

[9] a) A. L. Thompson, A. E. Goeta, J. A. Real, A. Galet, M. C. Muñoz, *Chem. Commun.* **2004**, 1390–1391; b) V. A. Money, I. R. Evans, M. Halcrow, A. E. Goeta, J. A. K. Howard, *Chem. Commun.* **2003**, 158–159; c) M. Marchivie, P. Guionneau, J. A. K. Howard, G. Chastanet, J. F. Létard, A. E. Goeta, D. Chasseau, *J. Am. Chem. Soc.* **2002**, *124*, 194–195; d) J. Kusz, H. Spiering, P. Gütlich, *J. Appl. Crystallogr.* **2001**, *34*, 229–238; e) J. Kusz, H. Spiering, P. Gütlich, *J. Appl. Crystallogr.* **2000**, *33*, 201–205.

[10] H. Brunner, A. Hollman, B. Nuber, M. Zabel, *J. Organomet. Chem.* **2001**, *633*, 1–6.

[11] a) T. Soma, T. Iwamoto, *Chem. Lett.* **1994**, 821–824; b) T. Soma, H. Yuge, T. Iwamoto, *Angew. Chem.* **1994**, *106*, 1750–1751; *Angew. Chem. Int. Ed. Engl.* **1994**, *33*, 1665–1666.

[12] C. J. Shorrock, B. Y. Xue, P. B. Kim. R. J. Batchelor, B. O. Patrick, D. B. Leznoff, *Inorg. Chem.* **2002**, *41*, 6743–6753.

[13] A. G. Sharpe, *The Chemistry of the Cyano Complexes of Transition Metals*, Academic Press, London, **1976**, p. 269.

[14] L. H. Jones, R. A. Penneman, *J. Chem. Phys.* **1954**, *22*, 965–970.

[15] S. Decurtins, P. Gütlich, C. P. Köhler, H. Spiering, A. Hauser, *Chem. Phys. Lett.* **1984**, *105*, 1–4.

[16] a) F. Lloret, M. Julve, J. Cano, G. De Munno, *Mol. Cryst. Liq. Cryst.* **1999**, *334*, 569–585; b) F. Lloret, G. De Munno, M. Julve, J. Cano, R. Ruiz, A. Caneschi, *Angew. Chem.* **1998**, *110*, 143–145; *Angew. Chem. Int. Ed. Engl.* **1998**, *37*, 135–138.

[17] T. Balic-Zunic, I. Vickovic, *J. Appl. Crystallogr.* **1996**, *29*, 305–306.

[18] M. Jansen, *Angew. Chem.* **1987**, *99*, 1100–1112; *Angew. Chem. Int. Ed. Engl.* **1987**, *26*, 1098–1110.

[19] A. F. Wells, *Three-Dimensional Nets and Polyhedra*, Wiley, New York, **1977**.

[20] H. Köppen, E. W. Müller, C. P. Köhler, H. Spiering, E. Meissner, P. Gütlich, *Chem. Phys. Lett.* **1982**, *91*, 348–352.

[21] a) B. A. Katz, C. E. Strouse, *J. Am. Chem. Soc.* **1979**, *101*, 6214–6221; b) M. Mikami, M. Konno, Y. Saito, *Chem. Phys. Lett.* **1979**, *63*, 566–569; c) L. Wiehl, G. Kiel, C. P. Köhler, H. Spiering, P. Gütlich, *Inorg. Chem.* **1986**, *25*, 1565–1571.

[22] D. Chernyshov, M. Hostettler, K. W. Törnroos, H.-B. Bürgi, *Angew. Chem.* **2003**, *115*, 3955–3960; *Angew. Chem. Int. Ed.* **2003**, *42*, 3825–3830; .

[23] A. Hauser, J. Jeftic, H. Romstedt, R. Hinek, H. Spiering, *Coord. Chem. Rev.* **1999**, *190–192*, 471–491.

[24] a) V. Petrouleas, J. P. Tuchagues, *Chem. Phys. Lett.* **1987**, *137*, 21–25; b) D. Boinnarad, A. Bousseksou, A. Dworkin, J. M. Savariault, F. Varret, J. P. Tuchages, *Inorg. Chem.* **1994**, *33*, 271–281.

[25] D. L. Reger, C. A. Little, V. G. Young Jr., M. Pink, *Inorg. Chem.* **2001**, *40*, 2870–2874.

[26] a) J. A. Real, J. Zarembowitch, O. Kahn, X. Solans, *Inorg. Chem.* **1987**, *26*, 2939–2943; b) J. A. Real, H. Bolvin, A. Bousseksou, A. Dworkin, O. Kahn, F. Varret, J. Zarembowitch, *J. Am. Chem. Soc.* **1992**, *114*, 4650–4658; c) J. A. Real, I. Castro, A. Bousseksou, M. Verdaguer, R. Burriel, M. Castro, J. Linares, F. Varret, *Inorg. Chem.* **1997**, *36*, 455–464; d) V. Ksenofontov, A. B. Gaspar, J. A. Real, P. Gütlich, *J. Phys. Chem. B* **2001**, *105*, 12266–12271.

[27] a) A. B. Gaspar, A. L. Thompson, M. C. Muñoz, A. E. Goeta, J. A. Real, unpublished results; b) V. Ksenofontov, A. B. Gaspar, V. Niel, S. Reiman, J. A. Real, P. Gütlich, *Chem. Eur. J.* **2004**, *10*, 1291–1298; c) N. Ortega-Villar, A. L. Thompson, R. Moreno-Esparza, V. Niel, A. B. Gaspar, M. C. Muñoz, A. E. Goeta, J. A. Real, *VIIIth International Conference on Molecule-based Magnets, ICMM2002*, C33, Valencia (Spain), 5–10 October **2002**.

[28] Y. García, O. Kahn, L. Rabardel, B. Chansou, L. Salmon, J. P. Tuchages, *Inorg. Chem.* **1999**, *38*, 4663–4670.

[29] V. Ksenofontov, H. Spiering, S. Reiman, Y. García, A. B. Gaspar, N. Moliner, J. A. Real, P. Gütlich, *Chem. Phys. Lett.* **2001**, *348*, 381–386.

[30] M. Sorai, S. Seki, *J. Phys. Chem. Solids* **1974**, *35*, 555–570.

[31] a) C. P. Slichter, H. G. Drickamer, *J. Chem. Phys.* **1972**, *56*, 2142–2160;; b) H. Spiering, E. Meissner, H. Köppen, E. W. Müller, P. Gütlich, *Chem. Phys.* **1982**, *68*, 65–71; c) H. Spiering, N. Willenbacher, *J. Phys. Condens. Matter* **1989**, *1*, 10089–10105.

[32] A. Desaix, O. Roubeau, J. Jeftic, J. Haasnoot, K. Boukheddaden, E. Codjovi, J. Linares, M. Nogues, F. Varret, *Eur. Phys. J. B* **1998**, *6*, 183–193.

[33] J. F. Létard, P. Guionneau, L. Rabardel, J. A. K. Howard, A. E. Goeta, D. Chasseau, O. Kahn, *Inorg. Chem.* **1998**, *37*, 4432–4441.

[34] J. Cosier, A. M. Glazer, *J. Appl. Crystallogr.* **1986**, *19*, 105–107.

[35] A. E. Goeta, L. K. Thompson, C. L. Sheppard, S. S. Tandon, C. W. Lehmann, J. Cosier, C. Webster, J. A. K. Howard, *Acta Crystallogr. Sect. C* **1999**, *55*, 1243–1246; Oxford Cryosystems Newsletter, Issue 2, August **2003**.

[36] A. L. Thompson, A. Beeby, A. E. Goeta, *J. Appl. Crystallogr.* **2004**, *37*, 652–653.

[37] SMART NT/2000, Data Collection Software, version 5.629; Bruker Analytical X-ray Instruments Inc., Madison, WI (USA), **2003**.

[38] SAINT+, Data Reduction Software, version 6.45 A; Bruker Analytical X-ray Instruments Inc., Madison, WI (USA), **2003**.

[39] TWINABS, Bruker Nonius scaling and corrections for twinned crystals, version 1.05, Bruker Analytical X-ray Instruments Inc., Madison, WI (USA), **2003**.

[40] SHELXTL NT/2000, version 6.14, Bruker Analytical Instruments Inc., Madison, WI, USA, **2003**.